

CBCT scatter correction with dual-layer flat-panel detector

Xin Zhang,^{1,2, a)} Jixiong Xie,^{3, a)} Ting Su,¹ Jiongtao Zhu,¹ Han Cui,¹ Yuhang Tan,¹
Dongmei Xia,^{3, b)} Hairong Zheng,^{4,5,6} Dong Liang,^{4,5} and Yongshuai Ge^{1,4,5,6, b)}

¹⁾*Research Center for Advanced Detection Materials and Medical Imaging Devices, Shenzhen Institute of Advanced Technology, Chinese Academy of Sciences, Shenzhen, Guangdong 518055, China*

²⁾*University of Chinese Academy of Sciences, Beijing 100049, China*

³⁾*Key Laboratory of Low-grade Energy Utilization Technologies and Systems of Ministry of Education of China, College of Power Engineering, Chongqing University, Chongqing 400044, China*

⁴⁾*Paul C Lauterbur Research Center for Biomedical Imaging, Shenzhen Institute of Advanced Technology, Chinese Academy of Sciences, Shenzhen, Guangdong 518055, China*

⁵⁾*Key Laboratory of Biomedical Imaging Science and System, Chinese Academy of Sciences, Shenzhen, Guangdong 518055, China*

⁶⁾*National Innovation Center for Advanced Medical Devices, Shenzhen, Guangdong 518131, China.*

(Dated: 12 August 2024)

Background: Recently, the popularity of dual-layer flat-panel detector (DL-FPD) based dual-energy cone-beam CT (DE-CBCT) imaging has been increasing. However, the image quality of DE-CBCT remains constrained by the Compton scattered X-ray photons.

Purpose: The objective of this study is to develop an energy-modulated scatter correction method for DL-FPD based CBCT imaging.

Methods: The DLFPD can measure primary and Compton scattered X-ray photons having different energies: X-ray photons with lower energies are predominantly captured by the top detector layer, while X-ray photons with higher energies are primarily collected by the bottom detector layer. Afterwards, the scattered X-ray signals acquired on both detector layers can be analytically retrieved via a simple model along with several pre-calibrated parameters. Both Monte Carlo simulations and phantom experiments are performed to verify this energy-modulated scatter correction method utilizing DL-FPD.

Results: Results demonstrate that the proposed energy-modulated scatter correction method can significantly reduce the shading artifacts of both low-energy and high-energy CBCT images acquired from DL-FPD. On average, the image non-uniformity is reduced by over 77% in the low-energy CBCT image and by over 66% in the high-energy CBCT image. Moreover, the accuracy of the decomposed multi-material results is also substantially improved.

Conclusion: In the future, Compton scattered X-ray signals can be easily corrected for CBCT systems using DL-FPDs.

Keywords: Scatter correction, CBCT imaging, Dual-layer flat-panel detector

^{a)}Xin Zhang and Jixiong Xie have made equal contributions to this work and are considered as the first authors.

^{b)}Scientific correspondence should be addressed to Dongmei Xia (xiadm@cqu.edu.cn) and Yongshuai Ge (ys.ge@siat.ac.cn).

I. INTRODUCTION

Recently, X-ray dual-energy cone-beam computed tomography (DE-CBCT) has attracted considerable research interest. Various data acquisition techniques have been developed to distinguish materials with more than two different materials. For example, the X-ray tube potential modulation (kVp switching) technique¹ and the dual-layer flat-panel detector (DL-FPD) based DE-CBCT imaging technique²⁻⁶. Compared to kVp switching, DL-FPD enables the acquisition of temporally synchronized dual-energy projections of the object at any gantry rotation angle. Consequently, material-specific CBCT images containing quantitative data are reconstructed. Similar to other FPD based CBCT imaging approach, the DL-FPD based DE-CBCT imaging is also susceptible to Compton scatter due to its large imaging area, e.g., $\geq 30 \text{ cm} \times 30 \text{ cm}$. Frequently, Compton scattered X-ray photons induce prominent shading artifacts at the center of reconstructed CBCT images, resulting in a significant degradation of image quality. In DL-FPD based DE-CBCT imaging, these shading artifacts would additionally deteriorate the accuracy of the decomposed basis images. Moreover, the scattered X-ray photons would introduce several other undesired effects to CT images beyond shading artifacts. For instance, streaking artifacts between two dense objects with high attenuation coefficients⁷ and pseudo-enhancement of renal cysts⁸.

To date, numerous studies have been conducted aiming to correct the Compton-scattered X-ray signals in CBCT imaging. Generally, these methods can be categorized into two groups: hardware-assisted corrections and computation-assisted corrections. Among the hardware-assisted approaches, the placement of an anti-scatter grid⁹ over the entire detector plane stands as the simplest and most widely used method to reject the scattered X-ray photons. Grids with higher ratios can reject more scatter, however, increasing the grid ratio may also result in an increased radiation dose to the patient due to the absorption of primary X-ray photons by the lead strips. The introduction of other devices can also facilitate the CBCT imaging scatter correction. For example, the beam blocker¹⁰⁻¹³ can be used to measure the amount of scattered X-ray photons on the detector plane. The beam-stop array (BSA)¹⁴⁻¹⁷ and primary modulator¹⁸⁻²⁰ are also helpful in scatter estimation. Nevertheless, the requirement for two repeated scans¹⁰ makes the implementation of the aforementioned methods challenging in clinical practice. This difficulty arises from the prolonged imaging time^{11,17}, increased radiation dose and potential system vibrations^{18,19}.

In addition, increasing the air gap^{9,21} between the object and the detector can also reduce the scattered X-ray signals. However, this may result in an overall increase of the system’s total length if keeping the same imaging field size, i.e., same magnification ratio.

On the other hand, the computation-assisted scatter correction methods include the Monte Carlo (MC) simulation^{22–26}, kernel-based estimation^{27–32}, model-based estimation^{33–35}, and deep learning approach^{36–39}. Specifically, MC simulations represent the most accurate approach for scatter estimation and can also be utilized for scatter correction in megavoltage CBCT imaging⁴⁰. To enhance computational efficiency, graphics processing units (GPUs) are harnessed to expedite particle transportation calculations²⁴. Furthermore, noise reduction algorithms are employed to optimize simulation time²². The kernel-based methods, known as scatter kernel superposition (SKS), estimate scatter by convolving the primary signal with a predetermined kernel obtained through MC simulations. The effectiveness of kernel-based SKS approaches has been demonstrated in both kilovoltage diagnostic and megavoltage treatment²⁹ CBCT applications. However, kernel-based methods encounter challenges in accurately capturing variations in object thickness or material composition due to their inherent assumption of symmetric kernel shapes²⁹. Asymmetric kernels^{31,32} could offer more precise estimations of scatter distribution, though the accuracy heavily depends on the size of the selected kernel segments. The model-based methods estimate the scatter distribution iteratively^{33–35}, and the performance may also rely on the assumed scatter model and the quality of image segmentation. Most recently, deep learning techniques are employed to obtain the scatter distributions^{37–39}. Still, their performance strictly depend on the quality and quantity of training data. As a result, implementing such data-driven approaches in practice is currently challenging, and further investigation is necessary.

In this study, a novel scatter artifact correction method is proposed for DL-FPD. Unlike the previously mentioned scatter estimation techniques, this approach does not rely on anti-scatter grids or time-consuming computations. The main idea of this new method is to estimate the distributions of scattered X-ray photons through separate measurements of detector responses at two distinct X-ray beam energies. We have named this method e-Grid, which is expected to significantly reduce shading scatter artifacts and enhance the accuracy of quantitative CBCT imaging performance.

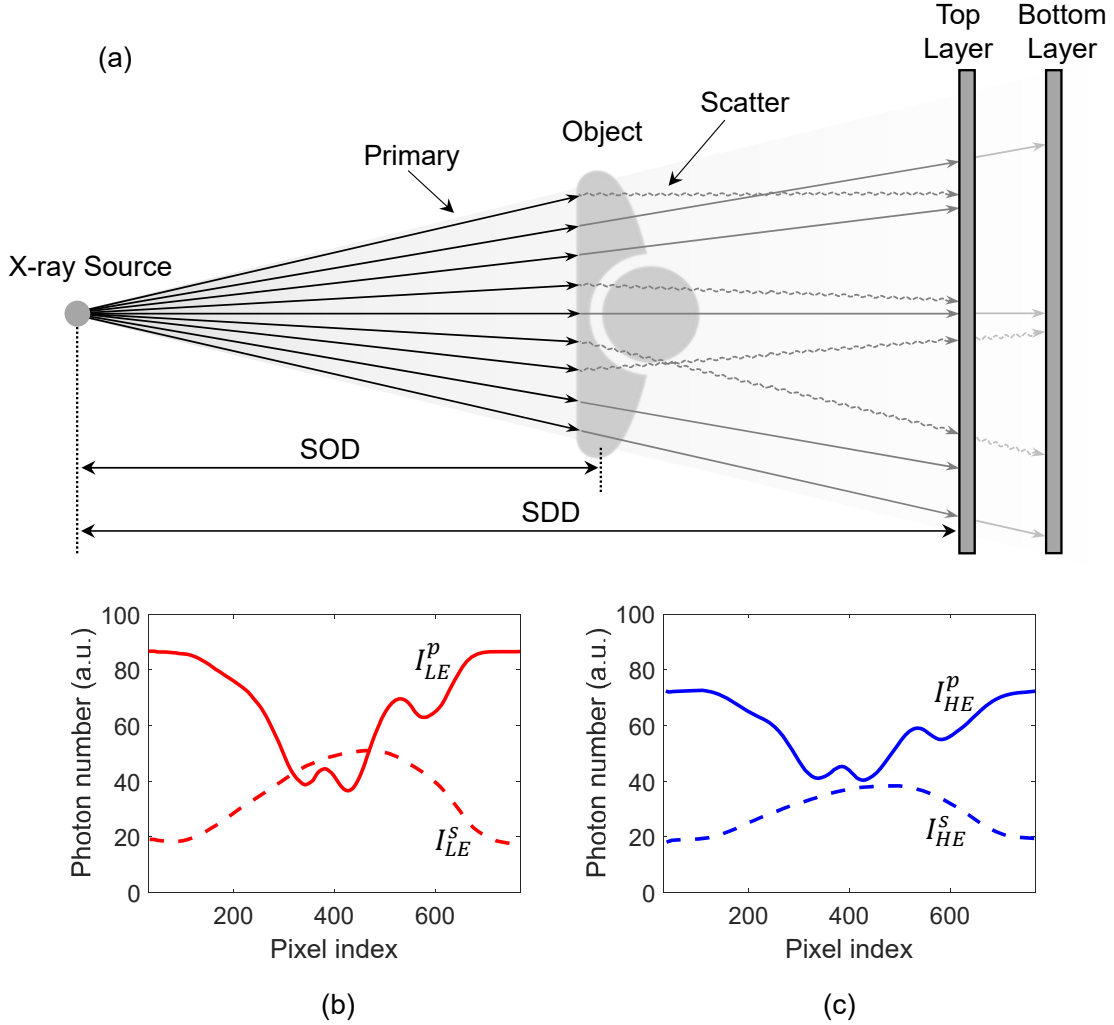


FIG. 1. (a) Illustration of CBCT setup with a dual-layer flat-panel detector. (b) The detected low-energy primary and scattered X-ray signals by the top layer. (c) The detected high-energy primary and scattered X-ray signals by the bottom layer. Optionally, a Copper filter can be placed between the top and bottom detector layers to enhance the spectral separation.

II. METHODS AND MATERIALS

A. Signal model

In the proposed e-Grid approach, it is assumed that the dual-energy X-ray intensities detected by the DL-FPD consist of two components: the primary X-ray signal and the Compton scattered X-ray signal, see Fig. 1. Mathematically, the low-energy (LE) signal

intensity I_{LE} and the high-energy (HE) signal intensity I_{HE} are expressed as:

$$I_{LE} = I_{LE}^p + I_{LE}^s, \quad (2.1)$$

$$I_{HE} = I_{HE}^p + I_{HE}^s, \quad (2.2)$$

where I_{LE}^p and I_{HE}^p denote the primary low-energy signal intensity and the primary high-energy signal intensity, respectively, I_{LE}^s and I_{HE}^s denote the scattered low-energy signal and the scattered high-energy signal, respectively.

To retrieve the scattered signals from the above two linear equations, the following approximations are assumed,

$$I_{LE}^p = f_p(I_{HE}^p) \approx \alpha_1^p I_{HE}^p + \alpha_0^p, \quad (2.3)$$

$$I_{LE}^s = f_s(I_{HE}^s) \approx \alpha_1^s I_{HE}^s + \alpha_0^s, \quad (2.4)$$

where function f_p and f_s are assumed to map the high-energy signals onto the low-energy signals⁴¹. Moreover, functions f_p and f_s are approximated by linear expansions with first-order coefficients α_1^p , α_1^s and zero-order coefficients α_0^p , α_0^s . By substituting Eq. (2.3) and Eq. (2.4) into Eq. (2.1), one gets:

$$I_{LE} \approx \alpha_1^p I_{HE}^p + \alpha_1^s I_{HE}^s + \alpha_0^p + \alpha_0^s, \quad (2.5)$$

By jointly solving Eq. (2.2) and Eq. (2.5), the high-energy scatter signal I_{HE}^s is found equal to:

$$I_{HE}^s = \frac{I_{LE} - \alpha_1^p I_{HE}^p - \alpha_0^p - \alpha_0^s}{\alpha_1^s - \alpha_1^p}. \quad (2.6)$$

Substituting Eq. (2.6) into Eq. (2.4), eventually, the low-energy scatter signal I_{LE}^s can be determined.

B. Signal processing

The entire workflow of the proposed scatter correction procedure is illustrated in Fig. 2. To estimate the parameters α_1^p , α_0^p , α_1^s and α_0^s , the calibration phantoms are scanned under two different experimental conditions: one with a cone beam (23 cm beam width on the detector plane) and the other with a fan beam (0.5 cm beam width on the detector plane). Since the measured scatter-to-primary ratios (SPR) are less than 7% for the two detector

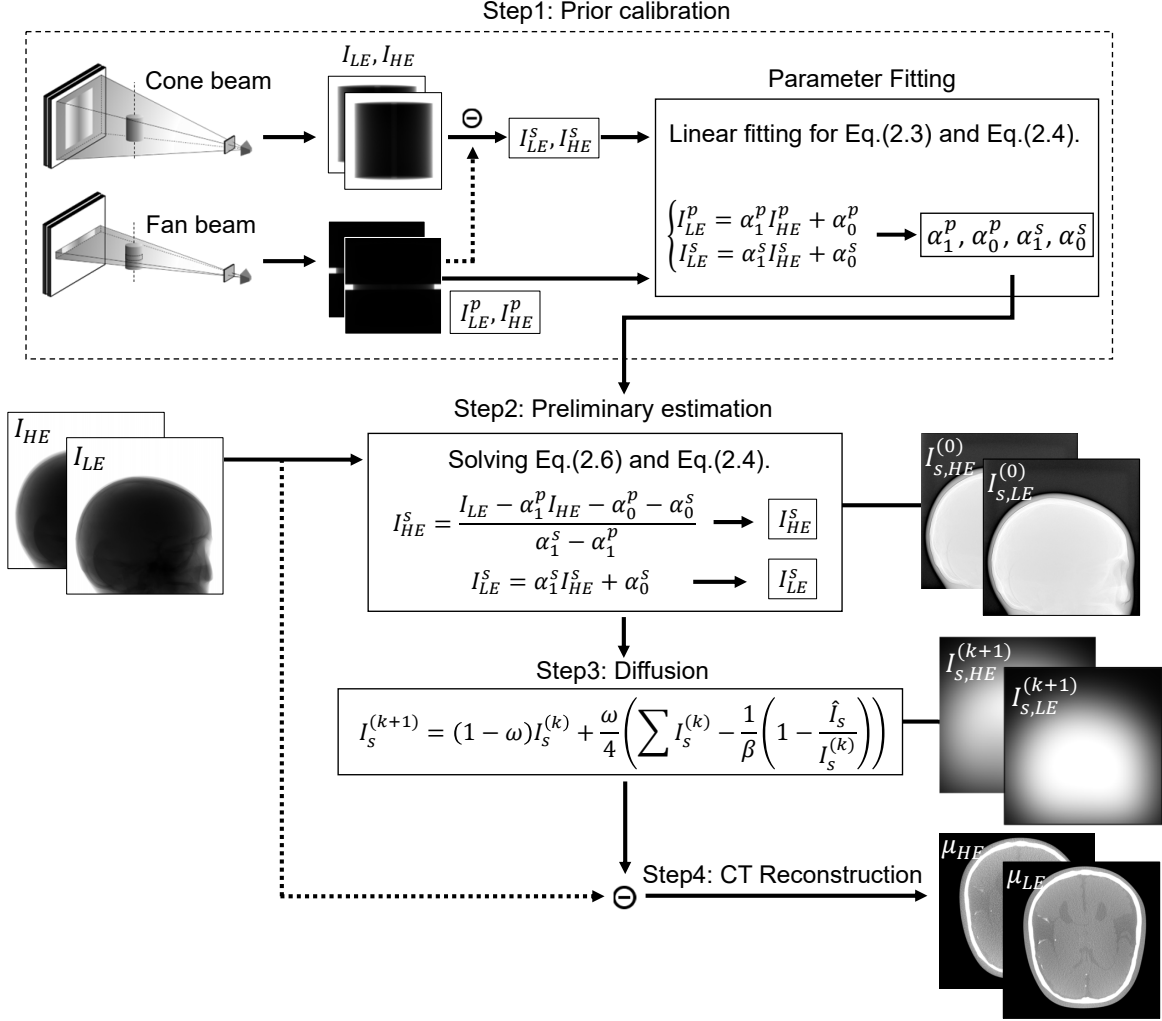


FIG. 2. The workflow of the proposed scatter correction method with DL-FPD. In the first step, parameters α_1^p , α_0^p , α_1^s and α_0^s are calibrated based on phantom measurements obtained from cone beam and fan beam imaging. In the second step, distributions of the scattered signals from the two detector layers are calculated, followed by diffusion of the high-frequency components in the third step. Finally, CBCT images without shading artifacts are reconstructed in the fourth step.

layers in the fan beam experiment, the scattered X-ray signal is neglected for the fan beam. In other words, the fan beam experiment only measures the primary signal I_{LE}^p and I_{HE}^p used in Eq. (2.3). On the contrary, both primary and scattered signals are measured simultaneously in the cone beam experiment, allowing the generation of the scatter-only signals I_{LE}^s and I_{HE}^s in Eq. (2.4). Finally, parameters α_1^p , α_0^p , α_1^s and α_0^s are determined through linear fittings, see Fig. 3 for more details. Specifically, a Polymethyl Methacrylate (PMMA,

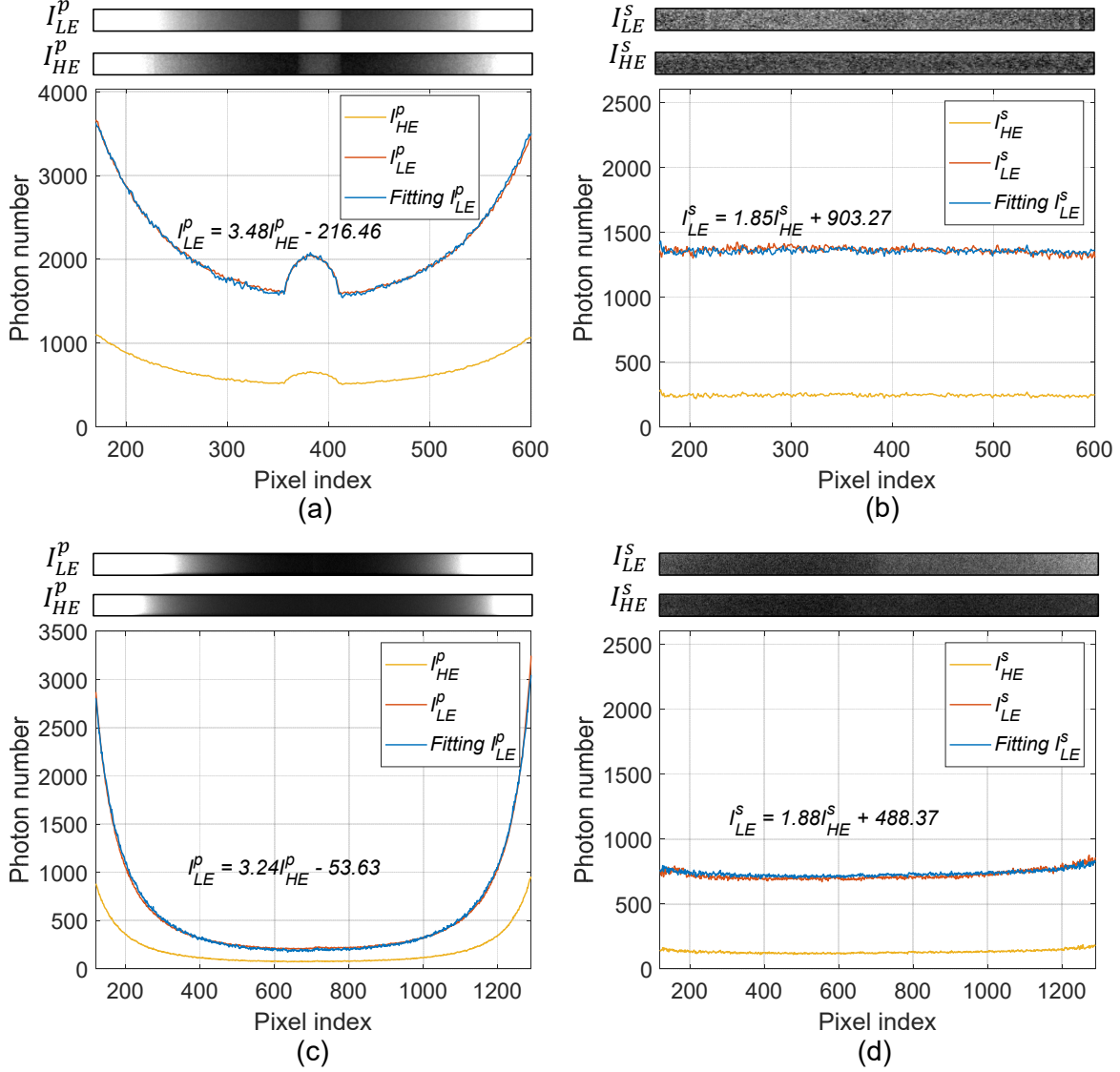


FIG. 3. Calibration results of the 16 cm PMMA phantom (a) the primary signal, $\alpha_1^p = 3.48$, $\alpha_0^p = -216.46$, (b) the scattered signal, $\alpha_1^s = 1.85$, $\alpha_0^s = 903.27$. Calibration results of the 30 cm water phantom (c) the primary signal, $\alpha_1^p = 3.24$, $\alpha_0^p = -53.63$, (d) the scattered signal, $\alpha_1^s = 1.88$, $\alpha_0^s = 488.37$.

mass density of 1.19 g/cm^3) cylinder phantom with a diameter of 16 cm is calibrated for head imaging, while a water cylinder phantom with a diameter of 30 cm is calibrated for body imaging.

In practice, some high-frequency structures are remained on the retrieved I_{LE}^s and I_{HE}^s images. To remove these residual high frequency components, an iterative diffusion algorithm⁴²

is employed. Such post-processing is expressed as:

$$I_s^{(k+1)}(u, v) = (1 - \omega)I_s^{(k)}(u, v) + \frac{\omega}{4} \left(\sum I_s^{(k)}(u, v) - \frac{1}{\beta} \left(1 - \frac{\hat{I}_s(u, v)}{I_s^{(k)}(u, v)} \right) \right), \quad (2.7)$$

where (u, v) denotes the pixel index, $\sum I_s^{(k)}(u, v) = I_s^{(k)}(u - 1, v) + I_s^{(k)}(u, v - 1) + I_s^{(k)}(u + 1, v) + I_s^{(k)}(u, v + 1)$, $\hat{I}_s(u, v)$ denotes the estimated low-energy signal or high-energy scatter signal, k denotes the iteration step. In our studies, $\omega = 0.8$ and $\beta = 1 \times 10^3$ are utilized.

C. Monte Carlo simulation

Monte Carlo (MC) simulations were conducted on GATE (ver 9.2) platform^{43,44} to validate the feasibility of this newly proposed scatter correction method. The incident beam spectrum used in GATE is generated at 125 kVp tube potential with 0.4 mm Cu filtration. The source to detector distance (SDD) is fixed at 1200 mm, the source to iso-center distance (SOD) is fixed at 1130 mm, and a 10 cm diameter digital water phantom containing two 2.5 cm diameter inserts filled with iodine solution of 20 mg/ml concentration was imaged. More details of the MC simulation are shown in Table I and Table II.

TABLE I. Key setups of the Monte Carlo simulation following the AAPM TG-268 protocol⁴⁵.

Item	Description
Software	GATE v9.2 (Geant4 ⁴⁶ v11.1.1 and Root ⁴⁷ v6.26).
Hardware	Intel Xeon(R) Gold 6248R CPU @ 3.00GHz.
Physics and transport	The simulated physics is managed by the Geant4 Monte Carlo kernel, which is responsible for tracking particles in matter and processing physical interactions.
Histories statistical uncertainty	2.35×10^{11} events per projection.
Timing	Approximately 3750 seconds to run 1 projection.
Scored quantities	X-ray photon deposition events.
Validation	The results were verified by the experiments.

TABLE II. The key parameters used for MC simulations and experiments.

	MC	Experiments
Detector array	190×100	768×768
Detector element size (mm)	0.616	0.308
Projection views	360	450
Tube potential (kVp)	125	125
Tube current(mA)	-	7.1
Beam filtration: Cu (mm)	0.4	0.4
Extra filtration: Cu (mm)	1.0	1.0

D. Phantom experiments

Physical phantom experiments are conducted on our benchtop system, which is equipped with a medical-grade X-ray tube (G-242, Varex, USA) and a dual-layer FPD (560RF-DE, Careray, China), see Fig. 4(a). The X-ray tube voltage is fixed at 125 kVp with 12.5 mA tube current, and the X-ray beam is filtered by 0.4 mm Copper. The DL-FPD has 1536×1536 detector elements with a native pixel dimension of 0.154 mm \times 0.154 mm, corresponding to an effective field-of-view (FOV) of 23.65 cm \times 23.65 cm. During data acquisition, the 2×2 binning mode is applied. The CsI:Tl material is 0.26 mm thick on the top detector layer and 0.55 mm thick on the bottom detector layer. The top detector layer and bottom detector layer are 6.6 mm apart, and an additional 1.0 mm copper filtration is inserted between them to increase spectral separation. Three phantoms were scanned: a self-made water cylinder of 10 cm diameter, see Fig. 4(c); an angiographic head phantom (Model: 41309-300, Kyoto Kagaku, Japan) of 16 cm diameter, see Fig. 4(d); an abdominal phantom (Model: 057A, CIRS, USA) of 28 cm diameter, see Fig. 4(e). Inside the water cylinder, tubes 1 to 4 contain iodine solution with concentration of 20 mg/ml, 10 mg/ml, 5 mg/ml, and 2.5 mg/ml, respectively. Moreover, tubes 5 to 8 are filled with gadolinium solution with concentrations of 20 mg/ml, 10 mg/ml, 5 mg/ml, and 2.5 mg/ml, respectively. Specifically, the source to detector distance (SDD) is fixed at 1200 mm, while the source to iso-center distance (SOD) is 950 mm, 1050 mm and 910 mm for the water phantom, head phantom, and abdominal phantom, respectively. More details of the experiment setups are provided

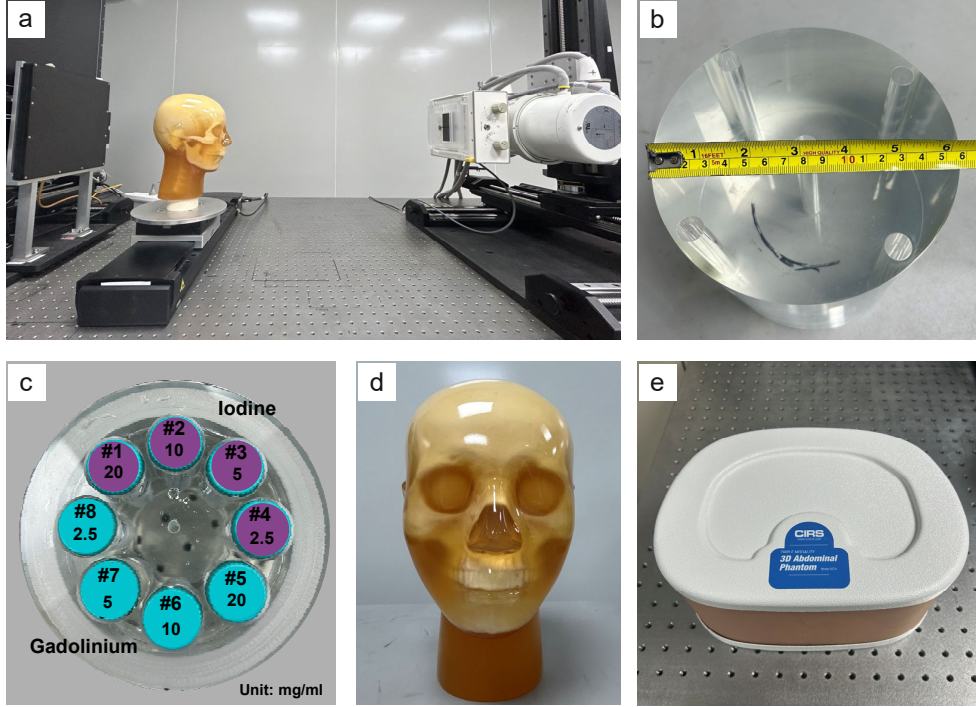


FIG. 4. (a) The experiment setup, (b) the PMMA cylinder phantom, (c) the water phantom with inserts of iodine and gadolinium solutions, (d) the head phantom, and (e) the abdominal phantom.

in Table II. To image the abdominal phantom, the detector was laterally shifted at two positions, each covering more than half of the phantom. Afterwards, dual-energy data of the entire abdominal phantom is stitched from the two sets of projections.

E. Evaluation metric

To quantify the correction performance, the image non-uniformity (NU) indices are measured. Explicitly, NU is defined as follows:

$$\text{NU} = \left| \frac{\bar{\mu}_c - \bar{\mu}_e}{\bar{\mu}_e} \right| \times 100\%, \quad (2.8)$$

where $\bar{\mu}_c$ and $\bar{\mu}_e$ denote the mean value of the region of interest (ROI) selected at the center and at the edge of the reconstructed CBCT images, respectively.

In addition, the signal-to-noise ratio (SNR) of the CT images was compared before and after scatter correction. The SNR of the CT images was defined as:

$$\text{SNR} = \frac{\bar{\mu}_s}{\sigma_n}, \quad (2.9)$$

where $\bar{\mu}_s$ denotes the mean value of the selected ROI on the reconstructed CT images, and σ_n denotes the corresponding standard deviation.

III. RESULTS

A. MC results

The MC simulation results are presented in Fig. 5. The projection containing total (primary and scatter) signals at a certain angle is presented in Fig. 5(a), while the scatter only signal I_{LE}^s is presented in Fig. 5(b). As seen, the scatter signal mainly consists of low-frequency components. However, the scatter signal $I_{LE}^{s,k=0}$ estimated from Eq. (2.4) and Eq. (2.6) contains clear residual structures of high frequency, see Fig. 5(c). The scatter distributions processed with Eq. (2.7) at four different iteration steps ($k = 100, 200, 300,$ and 400) are presented in Fig. 5(d)-(g), respectively. The line profiles in Fig. 5(h) demonstrate that diffusion can smooth out the structural residuals and generate a distribution similar to the ground truth at approximately 200 iterations.

The low-energy CT images reconstructed from the total signal, primary signal (ground truth), and scatter corrected signal are shown in Fig. 5(i)-(k), respectively. The high-energy CT images reconstructed from the total signal, primary signal (ground truth), and scatter corrected signal are shown in Fig. 5(m)-(o), respectively. Visually, the CBCT image reconstructed before scatter correction exhibits noticeable shading artifacts in the central region, indicating the presence of strong scatter artifacts. These shading artifacts are significantly reduced after processing with the proposed e-Grid method. Comparing to the ground truth, the e-Grid method produces similar results, as depicted in the profiles shown in Fig. 5(l) and Fig. 5(p). On the low-energy CT images, minor beam hardening artifacts are observed between the two iodine inserts.

B. Experimental results

The experimental results of the water phantom are shown in Fig. 6. The low-energy CT images are presented in the first row, while the high-energy CT images are presented in the second row. From left to right, the CT images are generated from cone beam, fan beam, and e-Grid (cone beam with scatter correction), respectively. As seen, CT images obtained

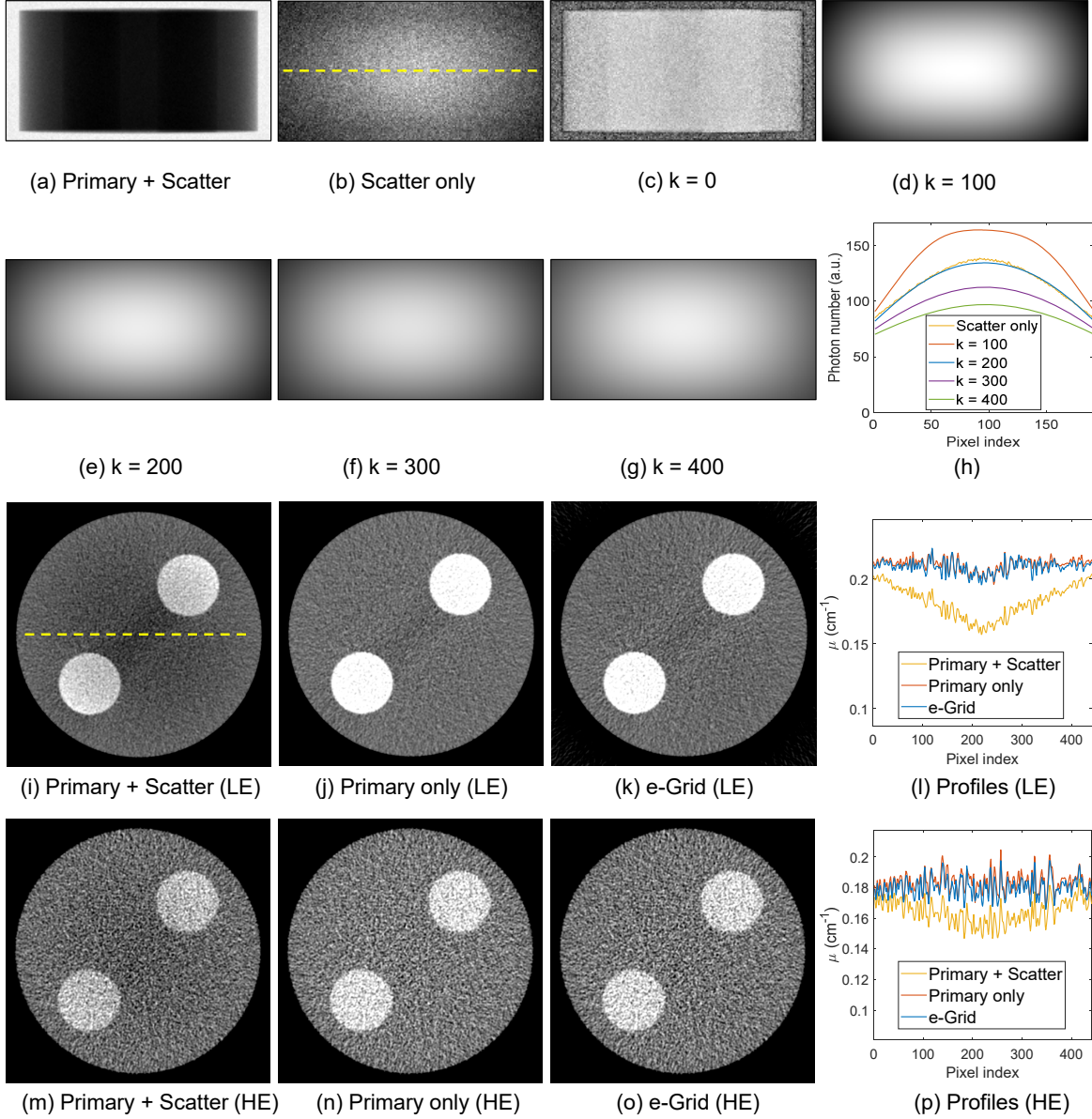


FIG. 5. The MC simulation results. (a) total signal, (b) scatter signal, (c) the calculated scatter signal before diffusion, (d)-(g) diffused projections with $k=100, 200, 300$ and 400 iterations, respectively, (h) line profile comparison results, (i)-(l) the low-energy CBCT imaging results. (m)-(p) the high-energy CBCT imaging results. The display window is $[0.11, 0.36] \text{ cm}^{-1}$ for the low-energy CT images, and $[0.09, 0.29] \text{ cm}^{-1}$ for the high-energy CT images.

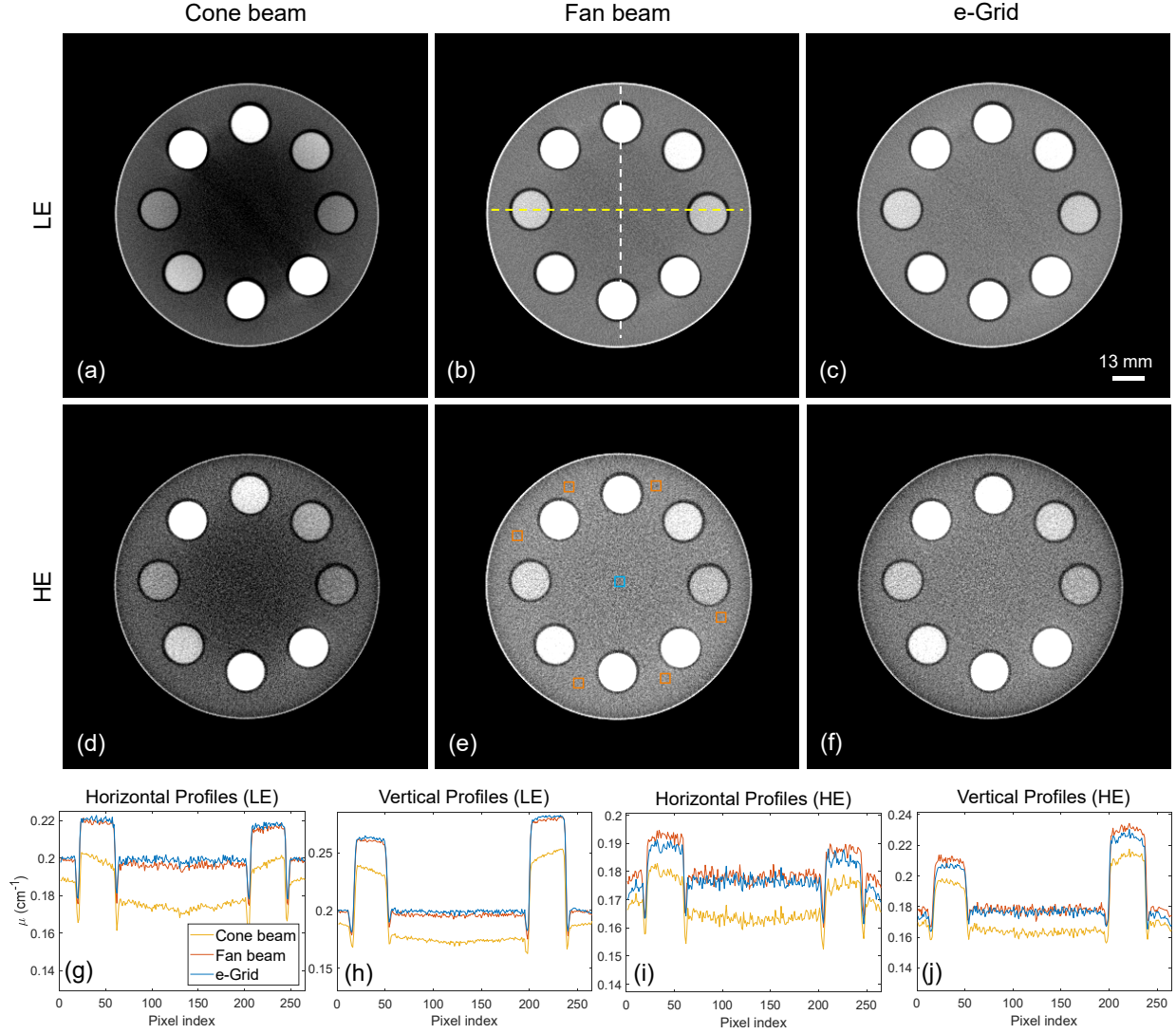


FIG. 6. Imaging results of the water cylinder phantom. The profiles along the horizontal and vertical directions are compared and plotted at the bottom. The display window is $[0.17, 0.23]$ cm^{-1} for low-energy CT, and $[0.15, 0.20]$ cm^{-1} for high-energy CT. The scale bar denotes 13 mm.

from cone beam exhibit pronounced shading artifacts before scatter correction, particularly noticeable in the low-energy CT image. Results indicate that narrowing the width of the X-ray beam can effectively mitigate the scatter-induced shading artifacts. Visually, the proposed e-Grid method can dramatically eliminate the scatter artifacts in both low-energy and high-energy CBCT images, resulting in a more uniform signal distribution. Based on the line profile results, it is evident that the e-Grid method is able to generate similar image quality in both horizontal and vertical directions when compared to the fan beam

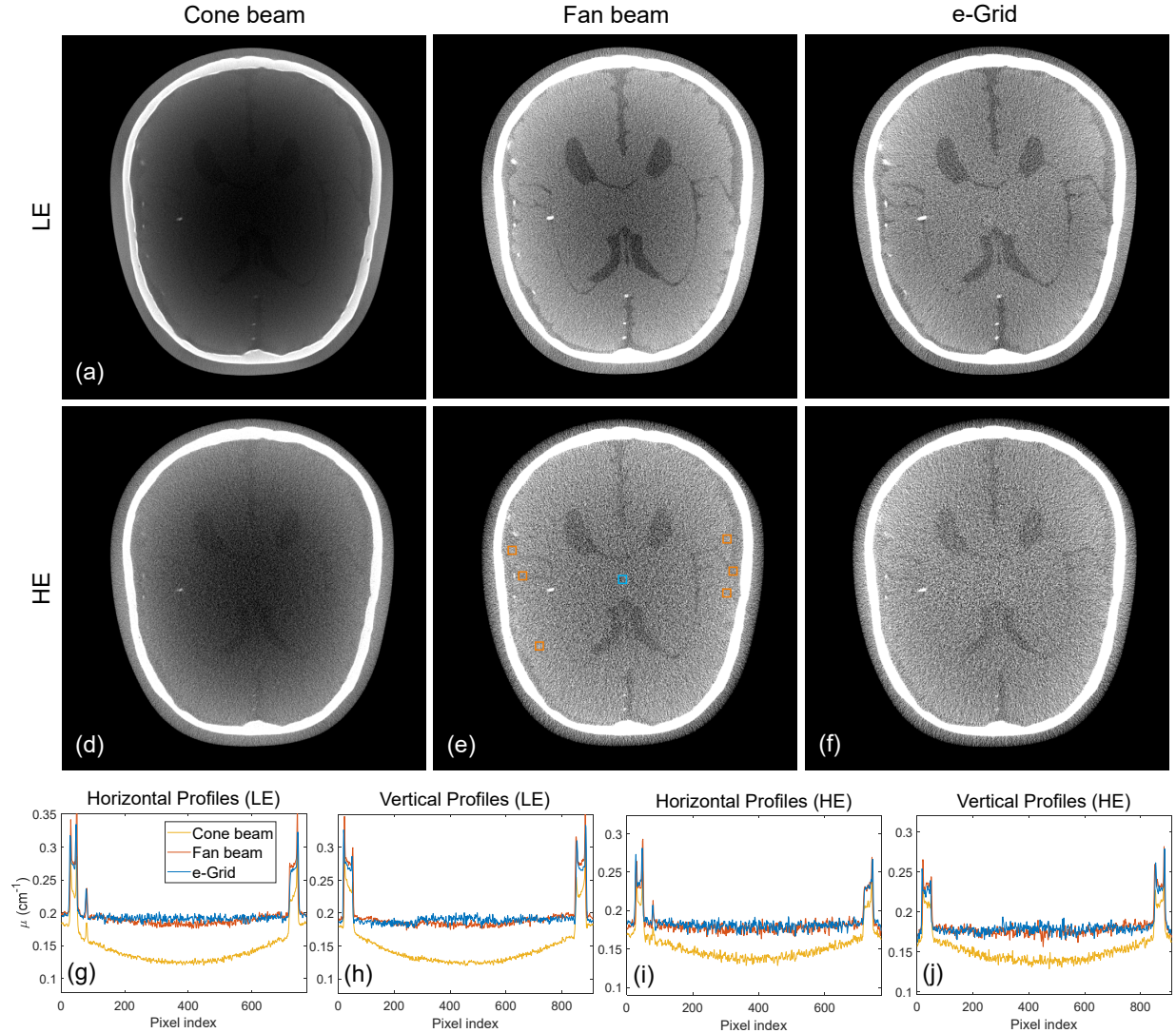


FIG. 7. Imaging results of the head phantom. The profiles along the horizontal and vertical directions are compared and plotted at the bottom. The display window is $[0.12, 0.25] \text{ cm}^{-1}$ for low-energy cone beam CT images, and $[0.17, 0.21] \text{ cm}^{-1}$ for low-energy fan beam and e-Grid CT images. The display window is $[0.13, 0.20] \text{ cm}^{-1}$ for high-energy cone beam CT images, and $[0.16, 0.20] \text{ cm}^{-1}$ for high-energy fan beam CT images and e-Grid processed CT images. The scale bar denotes 20 mm.

CT images. This is crucial for accurately quantifying the concentrations of iodine and gadolinium solution.

The experimental results of the head phantom are shown in Fig. 7 and Fig. 8. Clearly, distinguishing the brain tissue is challenging due to the presence of strong shading artifacts.

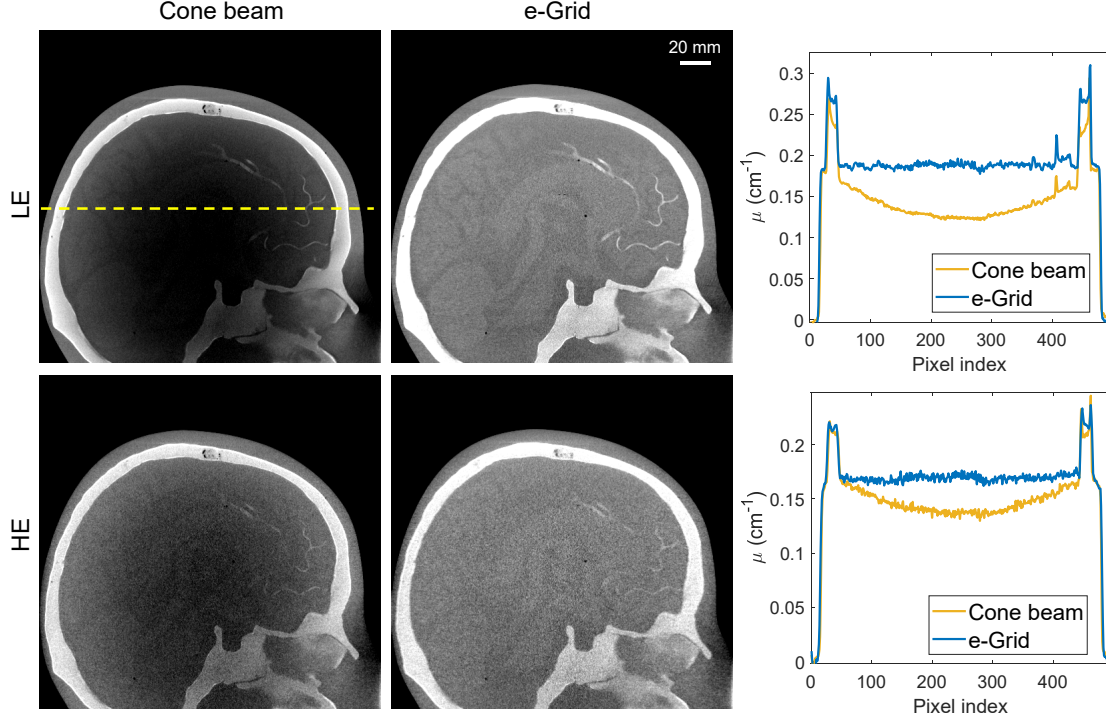


FIG. 8. Imaging results of head phantom on the sagittal view plane. The horizontal line profiles are presented on the right-hand side. The display window is $[0.12, 0.25] \text{ cm}^{-1}$ for low-energy CT images, and $[0.12, 0.22] \text{ cm}^{-1}$ for high-energy CT images. The scale bar denotes 20 mm.

The results demonstrate that the e-Grid method can effectively suppress the shading artifacts for both low-energy and high-energy CT images, see Fig. 8. As a result, the image quality and readability are significantly enhanced after processed by the e-Grid method.

The experiment results of the abdominal phantom are shown in Fig. 9. Compared to the water phantom and head phantom, the abdominal phantom has a larger diameter of 28 cm. Similarly, distinguishing tissues in the central region of the abdominal phantom before scatter correction is challenging. Reducing the beam width can help alleviate such shading artifacts. Obviously, the e-Grid method can also effectively mitigate the scatter artifacts in the CT images of the abdominal phantom. It performs well for both low-energy and high-energy CT imaging, see Fig. 9 (c) and (f). These results indicate that the proposed e-Grid method can be applied to correct the scatter shading artifacts of different object sizes.

Besides, image uniformity are measured, see the statistical results in Fig. 10. The selected ROIs for the water phantom, the head phantom and the abdominal phantom are

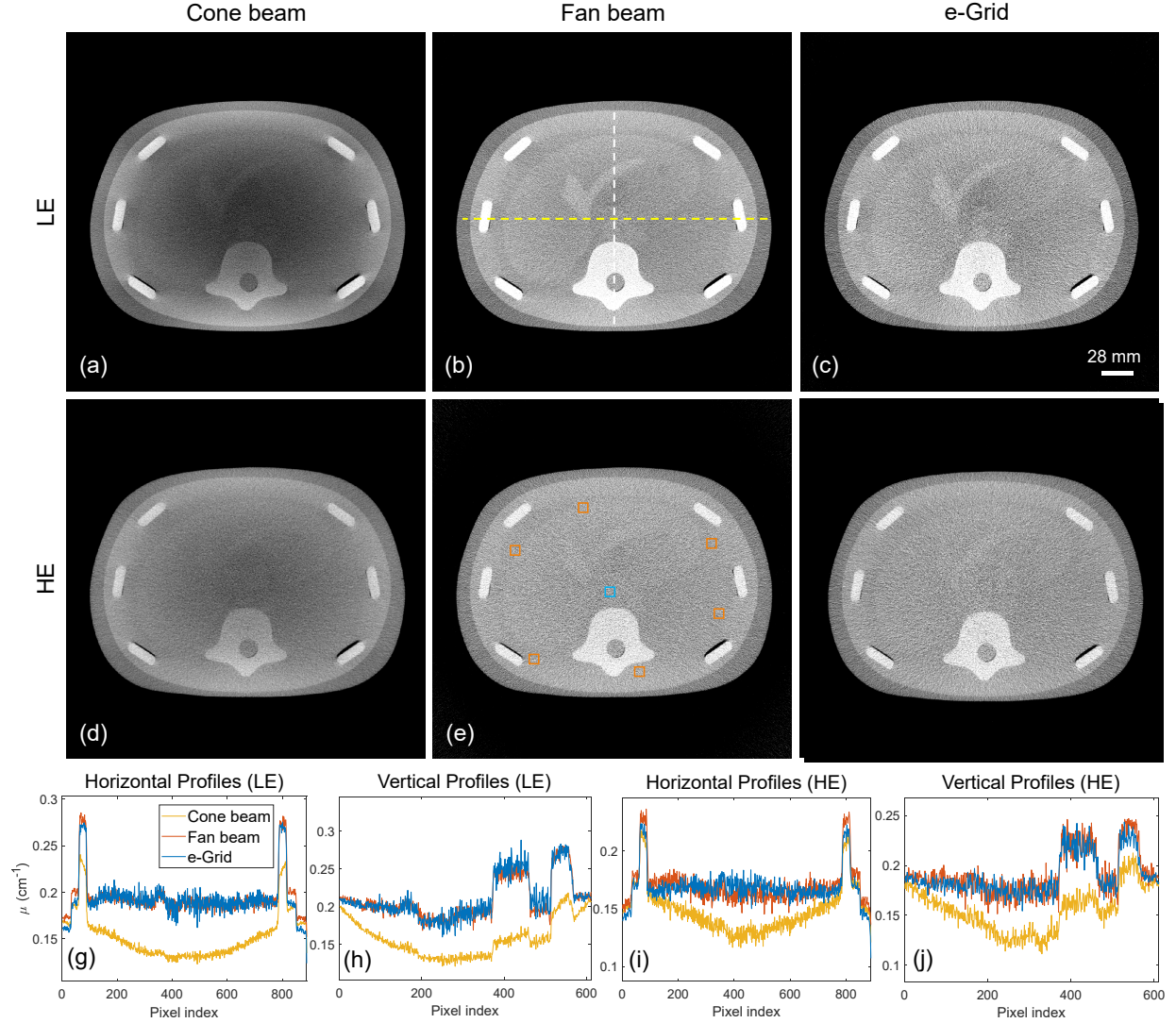


FIG. 9. Imaging results of the abdominal phantom. The profiles along the horizontal and vertical directions are compared and plotted at the bottom. The display window is $[0.10, 0.25] \text{ cm}^{-1}$ for low-energy CT images, and $[0.07, 0.24] \text{ cm}^{-1}$ for high-energy CT images. The scale bar denotes 28 mm.

shown in Fig. 6(e), Fig. 7(e) and Fig. 9(e), respectively. The blue-box area represents the central ROI, while the six orange-box areas represent the peripheral ROIs. Compared to the results obtained from cone beam setup, the NU value measured on the e-Grid processed low-energy CT images is reduced by over 87%, 90% and 77% for the water phantom, the head phantom, and the abdominal phantom, respectively. In addition, the NU value measured on the e-Grid processed high-energy CT images is reduced by over 66%, 92% and

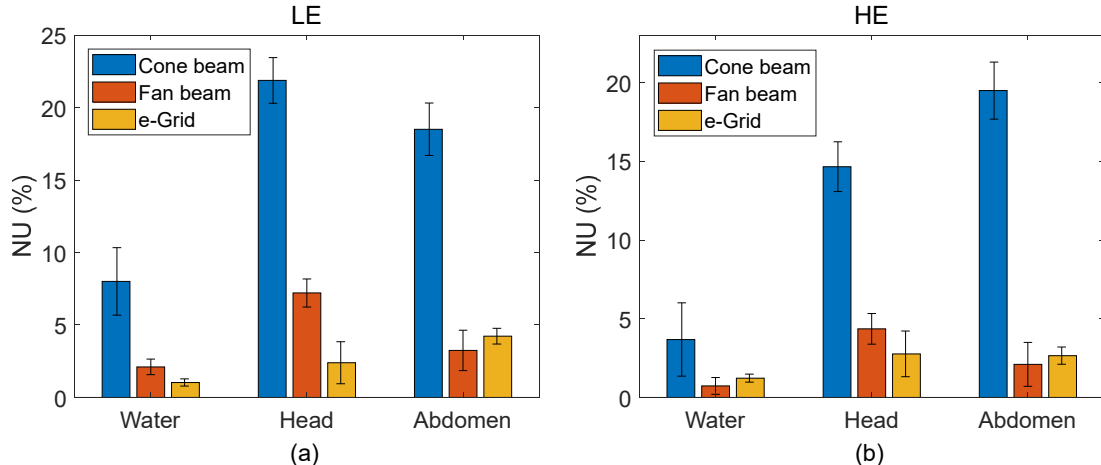


FIG. 10. The measured nonuniformity indices on the (a) low-energy CT images and (b) high-energy CT images for the water phantom, head phantom and abdominal phantom, respectively.

TABLE III. The measured SNR values for low-energy and high-energy CT images.

	Cone beam(LE)	e-Grid(LE)	Cone beam(HE)	e-Grid(HE)
Water phantom	54.23±5.07	49.65±4.28	33.72±1.90	32.53±1.75
Head phantom	48.72±4.47	38.77±5.16	34.23±5.27	29.27±3.55
Abdominal phantom	24.69±2.57	17.87±2.63	19.54±2.62	16.08±3.04

86% for the water phantom, the head phantom, and the abdominal phantom, respectively. These results demonstrate the effectiveness and robustness of the proposed e-Grid scatter correction method.

Finally, the measured SNR results are shown in Table III. The same ROIs were used for SNR measurements. Compared to the SNR before scatter correction, the SNR measured on the e-Grid processed low-energy CT images decreased by approximately 8%, 21% and 29% for the water phantom, the head phantom, and the abdominal phantom, respectively. Moreover, the SNR values measured on the e-Grid processed high-energy CT images decreased by approximately 4%, 18% and 18% for the water phantom, the head phantom, and the abdominal phantom, respectively. Be aware that such SNR reduction is due to the removal of the scattered X-ray photons.

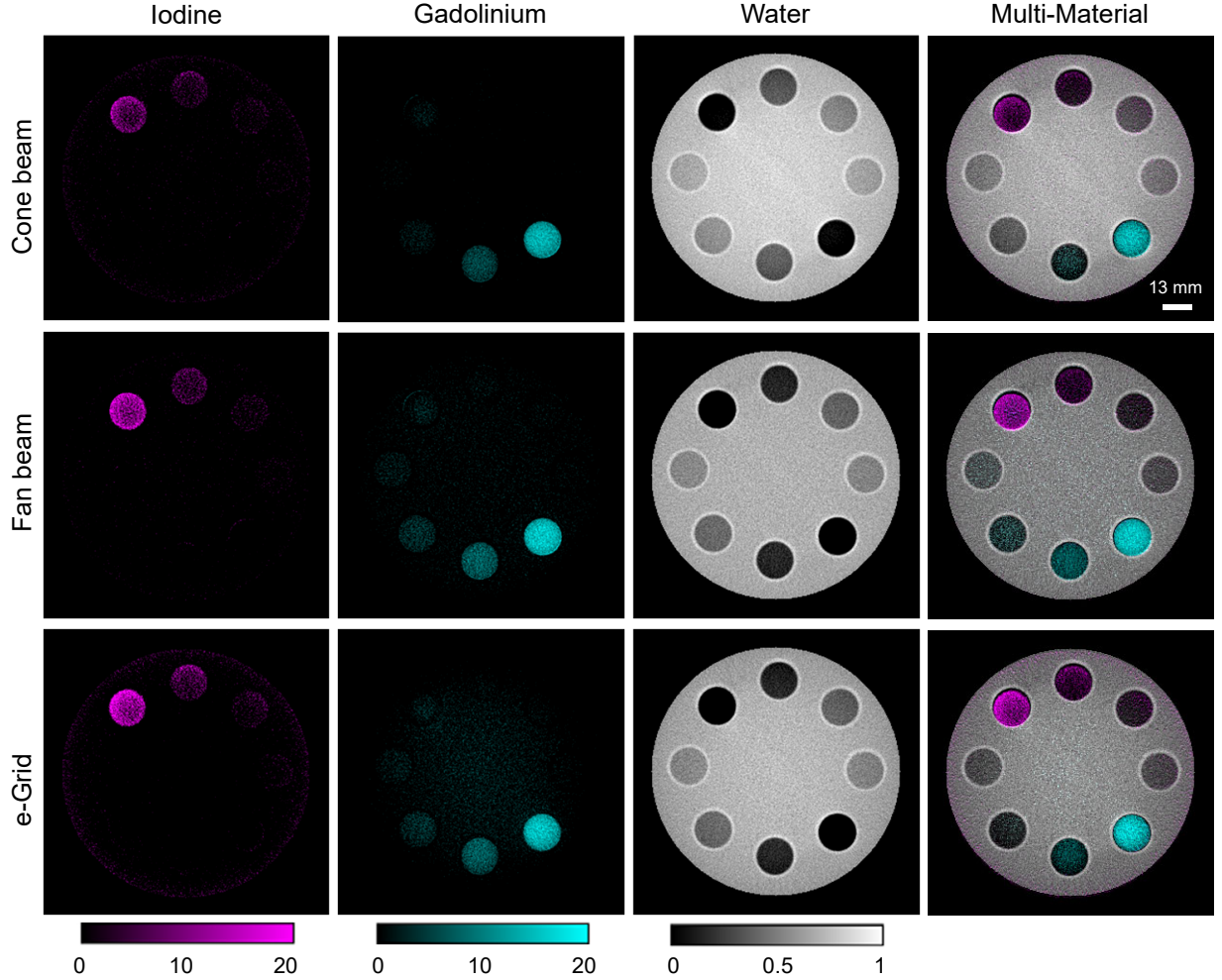


FIG. 11. The multi-material decomposition results of the water cylindrical phantom. From top to bottom, results correspond to the cone beam, fan beam and e-Grid corrected CT images. From left to right, images correspond to the iodine, gadolinium, water bases and color overlaid images. The scale bar denotes 13 mm.

C. Decomposition results

Material specific maps are generated from the low-energy and high-energy CT images using the multi-material decomposition algorithm (MMD)⁴⁸, see the results in Fig. 11. From top to bottom, results correspond to the uncorrected cone beam setup, the fan beam setup, and the e-Grid method. The decomposed iodine basis is marked in magenta, and the decomposed gadolinium basis is marked in cyan. Overall, the accuracy of the material bases before correction is low, see the measured material densities in Table IV. The number in

parentheses indicates the ground truth. The quantitative decomposition results of the iodine basis with the e-Grid method closely match the ground truth, demonstrating its enhanced performance in quantitative DE-CBCT imaging.

TABLE IV. Quantitative decomposition results of the water phantom.

Iodine (mg/ml)			Gadolinium (mg/ml)			Water (g/cm ³)		
Cone beam	Fan beam	e-Grid	Cone beam	Fan beam	e-Grid	Cone beam	Fan beam	e-Grid
12.823(20)	18.651(20)	19.568(20)	19.521(20)	21.085(20)	19.866(20)	1.159(1)	1.033(1)	1.062(1)
7.471(10)	9.406(10)	10.479(10)	8.640(10)	10.762(10)	10.342(10)	-	-	-
4.382(5)	4.810(5)	5.866(5)	3.259(5)	5.769(5)	5.249(5)	-	-	-
2.648(2.5)	2.093(2.5)	3.032(2.5)	0.636(2.5)	3.308(2.5)	2.883(2.5)	-	-	-

IV. DISCUSSIONS AND CONCLUSION

This study presents a novel scatter correction method, named e-Grid, for DL-FPD based CBCT imaging. With DL-FPD, two sets of primary and scattered X-ray signals can be measured independently at two distinct energy levels. Under a linear approximation, the low-energy and high-energy scattered signals can be estimated analytically. Consequently, scatter corrections can be performed easily for the dual-energy data acquired from the DL-FPD without the need of additional hardware such as anti-scatter grids. To validate the newly proposed e-Grid method, Monte Carlo simulation experiments and physical phantom experiments were conducted. Results demonstrate the high performance of the e-Grid scatter correction method in reducing the shading artifacts on the CBCT images. Quantitative analyses show that the e-Grid method is able to reduce the image non-uniformity by over 90% and 60% for the low-energy and high-energy CT images, respectively.

The assumptions made in Eqs. (2.3)-(2.4) are fundamental to the e-Grid method. An implicit requirement underlying Eqs. (2.3)-(2.4) is that the acquired low-energy and high-energy signal are spectrally distinct. With DL-FPD, such requirement can be easily satisfied, especially when an additional 1.0 mm thick copper filter is placed between the top and bottom detector layers. Additionally, this newly proposed e-Grid scatter correction method may also be applied in other dual-energy CBCT imaging systems that utilize dual X-ray sources

and detectors. For that specific dual-energy CBCT imaging setup, the acquired projections from the two individual source-detector systems should be accurately registered to minimize potential geometric inconsistencies. Finally, this proposed e-Grid scatter correction method may also be applicable to triple-layer FPDs.

The current study may have some limitations. Firstly, a group of pre-calibrated parameters α_1^p , α_0^p , α_1^s and α_0^s are valid only for objects having dimensions similar to those of the calibration phantom. For example, the parameters calibrated from a 16 cm PMMA phantom are valid for head imaging, whereas the calibrated parameters from the 32 cm PMMA phantom are valid for body or abdomen imaging. To image objects of other sizes, additional calibration experiments with phantoms of specific sizes should be conducted. Secondly, it has been observed that the removal of scatter signals leads to a slight increase in CT image noise. This occurs subtracting the scattered signals reduces the total number of X-ray photons. However, the decrease in SNR is relatively minor compared to the substantial improvements in image quality and the accuracy of subsequent quantitative decomposition. Thirdly, it would be interesting to investigate the scatter correction performance of the e-Grid approach with MeV X-ray beams in future studies with respect to applications of megavoltage image-guided radiation therapy^{29,40,49}. Fourth, objects with larger diameters, e.g., ≥ 35 cm, and objects having metal implants are interesting topics that need to be investigated in the future using DL-FPD based CBCT imaging.

In conclusion, a novel scatter correction method, named as e-Grid, is proposed for DL-FPD based CBCT imaging. It can quickly estimate the scattered signals from the acquired low-energy and high-energy projections. Experiments demonstrate that the e-Grid method can effectively reduce the shading artifacts, thereby significantly improving the quality of CBCT images and the accuracy of material decomposition. In the future, scatter corrections could be easily implemented in CBCT imaging systems using DL-FPD.

FUNDING

This work was supported in part by the National Natural Science Foundation of China (12027812, 62201560, 12305349, U23A20284, 12235006), Guangdong Basic and Applied Basic Research Foundation (2021TQ06Y108), Shenzhen Science and Technology Program (JSGGKQTD20210831174329010), Youth Innovation Promotion Association of Chinese

Academy of Sciences (2021362).

REFERENCES

- ¹K. Müller, S. Datta, M. Ahmad, J.-H. Choi, T. Moore, L. Pung, C. Niebler, G. Gold, A. Maier, and R. Fahrig, Interventional dual-energy imaging—Feasibility of rapid kV-switching on a C-arm CT system, *Medical Physics* **43**, 5537–5546 (2016).
- ²A. Vlassenbroek, Dual layer CT, *Dual Energy CT in Clinical Practice* , 21–34 (2011).
- ³N. Rassouli, M. Etesami, A. Dhanantwari, and P. Rajiah, Detector-based spectral CT with a novel dual-layer technology: principles and applications, *Insights Into Imaging* **8**, 589–598 (2017).
- ⁴M. Lu, A. Wang, E. Shapiro, A. Shiroma, J. Zhang, J. Steiger, and J. Star-Lack, Dual energy imaging with a dual-layer flat panel detector, in *Medical Imaging 2019: Physics of Medical Imaging*, volume 10948, pages 269–278, SPIE, 2019.
- ⁵O. Ozguner, A. Dhanantwari, S. Halliburton, G. Wen, S. Utrup, and D. Jordan, Objective image characterization of a spectral CT scanner with dual-layer detector, *Physics in Medicine & Biology* **63**, 025027 (2018).
- ⁶L. Shi, M. Lu, N. R. Bennett, E. Shapiro, J. Zhang, R. Colbeth, J. Star-Lack, and A. S. Wang, Characterization and potential applications of a dual-layer flat-panel detector, *Medical Physics* **47**, 3332–3343 (2020).
- ⁷P. M. Joseph and R. D. Spital, The effects of scatter in x-ray computed tomography, *Medical Physics* **9**, 464–472 (1982).
- ⁸J. Vetter and J. Holden, Correction for scattered radiation and other background signals in dual-energy computed tomography material thickness measurements, *Medical Physics* **15**, 726–731 (1988).
- ⁹U. Neitzel, Grids or air gaps for scatter reduction in digital radiography: a model calculation, *Medical Physics* **19**, 475–481 (1992).
- ¹⁰L. Zhu, Y. Xie, J. Wang, and L. Xing, Scatter correction for cone-beam CT in radiation therapy, *Medical Physics* **36**, 2258–2268 (2009).
- ¹¹J. Wang, W. Mao, and T. Solberg, Scatter correction for cone-beam computed tomography using moving blocker strips: A preliminary study, *Medical Physics* **37**, 5792–5800 (2010).

- ¹²T. Niu and L. Zhu, Scatter correction for full-fan volumetric CT using a stationary beam blocker in a single full scan, *Medical Physics* **38**, 6027–6038 (2011).
- ¹³H. Lee, L. Xing, R. Lee, and B. P. Fahimian, Scatter correction in cone-beam CT via a half beam blocker technique allowing simultaneous acquisition of scatter and image information, *Medical Physics* **39**, 2386–2395 (2012).
- ¹⁴L. A. Love and R. A. Kruger, Scatter estimation for a digital radiographic system using convolution filtering, *Medical Physics* **14**, 178–185 (1987).
- ¹⁵R. Ning, X. Tang, and D. Conover, X-ray scatter correction algorithm for cone beam CT imaging, *Medical Physics* **31**, 1195–1202 (2004).
- ¹⁶J. Siewerdsen, M. Daly, B. Bakhtiar, D. Moseley, S. Richard, H. Keller, and D. Jaffray, A simple, direct method for x-ray scatter estimation and correction in digital radiography and cone-beam CT, *Medical Physics* **33**, 187–197 (2006).
- ¹⁷L. Zhu, N. Strobel, and R. Fahrig, X-ray scatter correction for cone-beam CT using moving blocker array, in *Medical Imaging 2005: Physics of Medical Imaging*, volume 5745, pages 251–258, SPIE, 2005.
- ¹⁸J. S. Maltz, W.-E. Blanz, D. Hristov, and A. Bani-Hashemi, Cone beam X-ray scatter removal via image frequency modulation and filtering, in *2005 IEEE Engineering in Medicine and Biology 27th Annual Conference*, pages 1854–1857, IEEE, 2006.
- ¹⁹L. Zhu, N. R. Bennett, and R. Fahrig, Scatter correction method for x-ray CT using primary modulation: theory and preliminary results, *IEEE Transactions on Medical Imaging* **25**, 1573–1587 (2006).
- ²⁰L. Ritschl, R. Fahrig, M. Knaup, J. Maier, and M. Kachelrieß, Robust primary modulation-based scatter estimation for cone-beam CT, *Medical Physics* **42**, 469–478 (2015).
- ²¹J. H. Siewerdsen and D. A. Jaffray, Optimization of x-ray imaging geometry (with specific application to flat-panel cone-beam computed tomography), *Medical Physics* **27**, 1903–1914 (2000).
- ²²A.-P. Colijn and F. J. Beekman, Accelerated simulation of cone beam X-ray scatter projections, *IEEE Transactions on Medical Imaging* **23**, 584–590 (2004).
- ²³Y. Kyriakou, T. Riedel, and W. A. Kalender, Combining deterministic and Monte Carlo calculations for fast estimation of scatter intensities in CT, *Physics in Medicine & Biology* **51**, 4567 (2006).

- ²⁴A. Badal and A. Badano, Accelerating Monte Carlo simulations of photon transport in a voxelized geometry using a massively parallel graphics processing unit, *Medical Physics* **36**, 4878–4880 (2009).
- ²⁵Y. Xu, T. Bai, H. Yan, L. Ouyang, A. Pompos, J. Wang, L. Zhou, S. B. Jiang, and X. Jia, A practical cone-beam CT scatter correction method with optimized Monte Carlo simulations for image-guided radiation therapy, *Physics in Medicine & Biology* **60**, 3567 (2015).
- ²⁶A. Sisniega, W. Zbijewski, J. Xu, H. Dang, J. W. Stayman, J. Yorkston, N. Aygun, V. Koliatsos, and J. H. Siewerdsen, High-fidelity artifact correction for cone-beam CT imaging of the brain, *Physics in Medicine & Biology* **60**, 1415 (2015).
- ²⁷V. N. Hansen, W. Swindell, and P. M. Evans, Extraction of primary signal from EPIDs using only forward convolution, *Medical Physics* **24**, 1477–1484 (1997).
- ²⁸B. Ohnesorge, T. Flohr, and K. Klingenbeck-Regn, Efficient object scatter correction algorithm for third and fourth generation CT scanners, *European Radiology* **9**, 563–569 (1999).
- ²⁹J. S. Maltz, B. Gangadharan, S. Bose, D. H. Hristov, B. A. Faddegon, A. Paidi, and A. R. Bani-Hashemi, Algorithm for x-ray scatter, beam-hardening, and beam profile correction in diagnostic (kilovoltage) and treatment (megavoltage) cone beam CT, *IEEE Transactions on Medical Imaging* **27**, 1791–1810 (2008).
- ³⁰H. Li, R. Mohan, and X. R. Zhu, Scatter kernel estimation with an edge-spread function method for cone-beam computed tomography imaging, *Physics in Medicine & Biology* **53**, 6729 (2008).
- ³¹J. Star-Lack, M. Sun, A. Kaestner, R. Hassanein, G. Virshup, T. Berkus, and M. Oelhafen, Efficient scatter correction using asymmetric kernels, in *Medical Imaging 2009: Physics of Medical Imaging*, volume 7258, pages 644–655, SPIE, 2009.
- ³²M. Sun and J. Star-Lack, Improved scatter correction using adaptive scatter kernel superposition, *Physics in Medicine & Biology* **55**, 6695 (2010).
- ³³E. Meyer, C. Maaß, M. Baer, R. Raupach, B. Schmidt, and M. Kachelrieß, Empirical scatter correction (ESC): A new CT scatter correction method and its application to metal artifact reduction, in *IEEE Nuclear Science Symposium & Medical Imaging Conference*, pages 2036–2041, IEEE, 2010.

- ³⁴W. Zhao, S. Brunner, K. Niu, S. Schafer, K. Royalty, and G.-H. Chen, Patient-specific scatter correction for flat-panel detector-based cone-beam CT imaging, *Physics in Medicine & Biology* **60**, 1339 (2015).
- ³⁵W. Zhao, D. Vernekohl, J. Zhu, L. Wang, and L. Xing, A model-based scatter artifacts correction for cone beam CT, *Medical Physics* **43**, 1736–1753 (2016).
- ³⁶J. Maier, S. Sawall, M. Knaup, and M. Kachelrieß, Deep scatter estimation (DSE): Accurate real-time scatter estimation for X-ray CT using a deep convolutional neural network, *Journal of Nondestructive Evaluation* **37**, 1–9 (2018).
- ³⁷Y. Jiang et al., Scatter correction of cone-beam CT using a deep residual convolution neural network (DRCNN), *Physics in Medicine & Biology* **64**, 145003 (2019).
- ³⁸S. Kida, T. Nakamoto, M. Nakano, K. Nawa, A. Haga, J. Kotoku, H. Yamashita, and K. Nakagawa, Cone beam computed tomography image quality improvement using a deep convolutional neural network, *Cureus* **10** (2018).
- ³⁹C. Kurz, M. Maspero, M. H. Savenije, G. Landry, F. Kamp, M. Pinto, M. Li, K. Parodi, C. Belka, and C. A. Van den Berg, CBCT correction using a cycle-consistent generative adversarial network and unpaired training to enable photon and proton dose calculation, *Physics in Medicine & Biology* **64**, 225004 (2019).
- ⁴⁰L. Spies, M. Ebert, B. Groh, B. Hesse, and T. Bortfeld, Correction of scatter in megavoltage cone-beam CT, *Physics in Medicine & Biology* **46**, 821 (2001).
- ⁴¹S. Brunner, B. E. Nett, R. Tolakanahalli, and G.-H. Chen, Prior image constrained scatter correction in cone-beam computed tomography image-guided radiation therapy, *Physics in Medicine & Biology* **56**, 1015 (2011).
- ⁴²X. Jia, H. Yan, L. Cerviño, M. Folkerts, and S. B. Jiang, A GPU tool for efficient, accurate, and realistic simulation of cone beam CT projections, *Medical Physics* **39**, 7368–7378 (2012).
- ⁴³S. Jan et al., GATE: a simulation toolkit for PET and SPECT, *Physics in Medicine & Biology* **49**, 4543 (2004).
- ⁴⁴D. Sarrut et al., Advanced Monte Carlo simulations of emission tomography imaging systems with GATE, *Physics in Medicine & Biology* **66**, 10TR03 (2021).
- ⁴⁵I. Sechopoulos, D. W. Rogers, M. Bazalova-Carter, W. E. Bolch, E. C. Heath, M. F. McNitt-Gray, J. Sempau, and J. F. Williamson, RECORDS: improved reporting of monte Carlo RaDIation transport studies: report of the AAPM Research Committee Task Group

- 268, *Medical Physics* **45**, e1–e5 (2018).
- ⁴⁶S. Agostinelli et al., GEANT4—a simulation toolkit, *Nuclear instruments and methods in physics research section A: Accelerators, Spectrometers, Detectors and Associated Equipment* **506**, 250–303 (2003).
- ⁴⁷R. Brun and F. Rademakers, ROOT—An object oriented data analysis framework, *Nuclear instruments and methods in physics research section A: accelerators, spectrometers, detectors and associated equipment* **389**, 81–86 (1997).
- ⁴⁸P. R. Mendonça, P. Lamb, and D. V. Sahani, A flexible method for multi-material decomposition of dual-energy CT images, *IEEE Transactions on Medical Imaging* **33**, 99–116 (2013).
- ⁴⁹C. J. Boylan, T. E. Marchant, J. Stratford, J. Malik, A. Choudhury, R. Shrimali, J. Rodgers, and C. G. Rowbottom, A megavoltage scatter correction technique for cone-beam CT images acquired during VMAT delivery, *Physics in Medicine & Biology* **57**, 3727 (2012).